EES Batteries

ROYAL SOCIETY OF CHEMISTRY

PAPER

View Article Online
View Journal | View Issue

Cite this: *EES Batteries*, 2025, **1**, 1255

Unlocking high performance in a Na–Fe–Mn–O cathode through phase-transition-free cycling†

Amit Ghoshal,[a] Vikas Singh Thakur,[b] Susmita Pramanik,[a] Vanshika Mehta,[b] Sher Singh Meena,[c] Moritz Hirsbrunner,[d] S. D. Kaushik,[e] Tinku Dan,[f] Pontus Törnblom,[d] Laurent Duda,[d] Anirudha Ghosh,[g] Conny Såthe,[g] Takashi Tokushima,[g] Subham Ghosh,[a] Swastika Banerjee[b] and Urmimala Maitra *[a]

Received 30th May 2025,
Accepted 14th July 2025

DOI: 10.1039/d5eb00106d

rsc.li/EESBatteries

Fe–Mn-based Na-layered oxide cathodes suffer from severe phase transitions at high states of charge, accompanied by transition metal migration and large-volume collapse. We propose the incorporation of a small amount of Li^+ into the transition metal layer to enable phase-transition-free cycling across a wide state-of-charge (SOC) range. In contrast to the previously studied undoped or Li/Mg/Ni doped P2-type Na–Fe–Mn–O cathodes, our P2-$Na_{0.7}Li_{0.127}Fe_{0.127}Mn_{0.746}O_2$ (NLFM) cathode, which has optimized Li, Fe and Mn contents and a disordered transition-metal layer, exhibits the remarkable property of complete suppression of O-type layer formation up to the highest charge voltage of 4.5 V. The cathode demonstrates reversible high-voltage Fe and O redox reactions without any phase transition. The P to O phase transition, accompanied by transition-metal-migration and □–O–□ (□ = vacancy) formation, is essential for the activation of O-redox in undoped Fe–Mn cathodes. The highly ionic character of Li–O bonds in NLFM increases the electron density over the O orbitals, making O-redox feasible in the P2-phase even in the absence of □–O–□. By retaining its P2 phase at the highest state of charge, the cathode shows a negligible volume change of less than 1.8%, thereby yielding high energy density along with excellent retention. The improved electrochemical performance of the Li-doped cathode arises from dopant-induced static and dynamic disorder, ensuring structural stability across a wide SOC range.

Broader context

Na-ion batteries are the technology of choice for applications where cost and sustainability matter. P2-type layered oxides of Na offer the perfect combination of a dense crystal structure, high electrical conductivity and Na-diffusivity, and therefore high energy density. Of the many known P2-type cathodes, Na–Fe–Mn–O is the preferred choice due to its optimal balance of properties, including abundant precursor availability, cost-effectiveness, and high energy density. However, its widespread adoption has been hindered by unsatisfactory long-term cycling due to structural instabilities. This study shows that adding Li^+ as a dopant to the Na–Fe–Mn–O cathode stabilizes the P2 phase in both high- and low-Na stoichiometries. Without structural transitions or significant volume changes, the Li-doped cathode retains its high energy density over many cycles.

Introduction

Of the two most studied Na layered oxides, P2 (trigonal prismatic Na) cathodes with larger Na diffusion channels exhibit higher ionic conductance, improved reversible capacities and more air stability compared to the O3-type (octahedral Na) cathodes.[1] O3-Na layered oxides also suffer from rapid capacity fading due to multiple phase transitions during cycling and complicated Na diffusion pathways.[2,3] Considering the earth-abundance of Fe and Mn and the practicability of P2-type Na-cathodes, P2-Na–Fe–Mn–O cathodes are clearly the material of choice for low cost yet high energy density Na-ion batteries.[4,5] Unfortunately, these cathodes undergo a large volume collapse

[a]*School of Materials Sciences, Indian Association for the Cultivation of Science, 2A & 2B Raja S. C. Mullick Road, Jadavpur, Kolkata, India. E-mail: urmimala.maitra@iacs.res.in*
[b]*Department of Chemistry, Indian Institute of Technology Roorkee, Roorkee, Uttarakhand, India*
[c]*Solid State Physics Division, Bhabha Atomic Research Centre, Mumbai, India*
[d]*Department of Physics and Astronomy, Condensed Matter Physics of Energy Materials, Uppsala University, Uppsala, Sweden*
[e]*UGC-DAE Consortium for Scientific Research, Mumbai Centre, BARC Campus, Mumbai, India*
[f]*Deutsches Elektronen-Synchrotron (DESY), Notkestraße 85, 22607 Hamburg, Germany*
[g]*MAX IV Laboratory, Lund University, PO Box 118, SE-22100 Lund, Sweden*
† Electronic supplementary information (ESI) available. See DOI: https://doi.org/10.1039/d5eb00106d

of nearly 10–25% at the highest state of charge when they are converted to the O2 or OP4 phase, accompanied by transition metal (TM) migration.[6] This is exacerbated in the case of Fe-rich cathodes, where the Fe^{4+}–O_6 octahedra formed at the end of the charge are Jahn–Teller distorted and therefore highly susceptible to TM migration.[7,8] Fe^{4+} migrating to the O-type alkali metal (AM) layer gets partially trapped, resulting in the voltage hysteresis and capacity loss. Truncated cycling regions of 2.0–4.0 V can reduce the negative effects of the P2 to O2/OP4 transition and improve cycle life.[9] However, this improved cycle life comes at the expense of energy density. It is therefore imperative to look for ways to utilize the high voltage region without causing P to O layer gliding. Previous studies on substituting Ni^{2+} or Mg^{2+} with Fe^{3+} proved to be effective in partially reducing Fe^{4+} migration.[8,10] The materials still exhibited a significant P2–O2/OP4 phase transition with large volume changes in the range of 15%, which ultimately led to poor cycling performances.[6]

In this paper, we demonstrate that a Li dopant in the TM layer can stabilize the P2 phase for a wide range of Na compositions while preserving rapid Na-ion (de)intercalation kinetics. Notably, at a high SOC, *i.e.*, under desodiated conditions, Li^+ exhibits greater mobility than Fe^{4+}, migrating preferentially before Fe^{4+} or Mn^{4+}. As a result, during Na deintercalation, the dynamic Li^+ suppresses layer gliding and O-phase formation. This phenomenon persists up to Na stoichiometries as low as 0.21 moles. In contrast, undoped or Mg/Ni-doped layered cathodes favor the P-to-O transition due to the preferential occupation of Mg/Ni/Fe ions in tetrahedral sites within the O-type AM layer. These ions effectively anchor the O-type structure, preventing its reversion to the P-type during Na reinsertion.[8,10] The present study also demonstrates that the same dopant (Li^+) stabilizes the P2 phase (as opposed to the O3 phase) under conditions of high Na-stoichiometry, reaching up to 0.79 moles. Utilization of low-valence Li^+ ions necessitates an increase in the valence of Mn from +3 to +4. This leads to an overall increase in the cationic potential that stabilizes the P2 phase.

A substantial body of research has previously examined the efficacy of doping strategies in hindering the P2 to O2 phase transition but has failed to suppress the transition to an O and P stacked phase (also called the Z phase or the OP4 phase).[6] The novelty of the current work lies in the complete suppression of O-type layer formation. The work is also distinguished by the utilization of a sole dopant, Li^+, to extend the operational Na window in both the high- and low-Na stoichiometry directions while impeding structural phase transitions. The ionic Li–O–Na bond (compared to the TM–O–Na bond) in Li-doped cathodes promotes electron localization on the O, ensuring O-redox activity in the absence of the P-to-O phase transition. Reversible high-voltage O-redox in the P2 phase ensures high energy density, as well as high stability and efficiency.

Results and discussion

The P2 phase is known to be stable within the stoichiometric region of Na between $1/3 < x < 2/3$, particularly for Na–Fe–Mn–O cathodes, where x represents the number of moles of Na in one formula unit. We demonstrate that utilization of Li as a dopant extends the stability window of the P2 phase to at least $0.21 < x < 0.79$. Avoiding structural phase transitions over many charge–discharge cycles improves cyclic stability and minimizes volume change. First, we discuss the Li-doping approach to stabilize the P2 phase in the high-Na limit. Then, in later sections, we discuss how Li-doping also stabilizes the P2 phase in the low-Na limit.

Stabilizing high Na in P2-type Na–Li–Fe–Mn–O

The P2/O3 ratio in materials is determined by the interlayer distance of the O–Na–O layer in relation to its O–TM–O layer. According to the "cationic potential" theory developed by Zhao *et al.*, when the Φ_{TM} (defined as the weighted average of ionic potentials of all TMs) falls above the P2–O3 barrier line, the material undergoes a transition from P2 to O3.[11] Higher Φ_{TM} indicates better electron cloud delocalization and an increase in the interlayer repulsion, thereby favouring the P2-type structure. Conversely, at higher levels of Na (high Φ_{Na}) the presence of Na ions serves to mitigate the O–O repulsions within the O–Na–O layer, thereby promoting the O3 structure. As demonstrated in Fig. S1a,† for $Na_{0.67}Fe_{0.5}Mn_{0.5}O_2$, Φ_{Na} and Φ_{TM} are related such that they lie in the P2-region but at a close proximity to the P2–O3 phase transition barrier line of the Rouxel diagram. Experimental observations indicate that minute alterations to the synthesis conditions result in materials with a P2–O3 mixed phase.[12,13] According to this theory, a greater amount of Na can only be stabilized in the P2 structure by increasing the Φ_{TM}, which in turn requires an increase in the Mn^{4+} content and a decrease in the Fe^{3+} content. The incorporation of Li^+ facilitates this process. Employing this strategy, we have successfully stabilized the P2 structure with up to 0.8 moles of Na in the Na–Li–Fe–Mn–O system. Consequently, the cathode $Na_{0.8}[Li_{0.22}Fe_{0.14}Mn_{0.64}]O_2$ (designated as NLFM1) was positioned just below the P2–O3 barrier line in the Rouxel diagram (Fig. S1a†). To the best of our knowledge, this is the highest Na-containing composition reported for the Na–Li–Fe–Mn–O system in the pure P2 phase, as shown in Fig. 1a, upper panel. Rietveld refinement of NLFM1 was carried out using the $P6_3/mmc$ space group (Table S1†) and showed no detectable impurities. In a previous study, Yang *et al.* synthesized $Na_{4/5}[Li_{1/5}Fe_{1/5}Mn_{3/5}]O_2$ with a high Na content and comparable Li content, aiming for a pure P2 material.[14] However, their material consisted of mixed P2 and O3 phases since the cathode lies on the P2–O3 borderline in the Rouxel diagram (Fig. S1a†).

NLFM1 demonstrates charge and discharge capacities of 179/122 mAh g^{-1}, respectively, within the voltage range of 2.0 to 4.5 V at the C/10 rate, exhibiting a capacity retention of 76% after 50 cycles (Fig. S2c and S2d†). It is worth mentioning that the cationic potential of NLFM1 still lies in a close proximity to the P2–O3 barrier line in the Rouxel diagram. Therefore, it is imperative to exercise extreme caution during the synthesis process to ensure that the material is produced in its pure P2

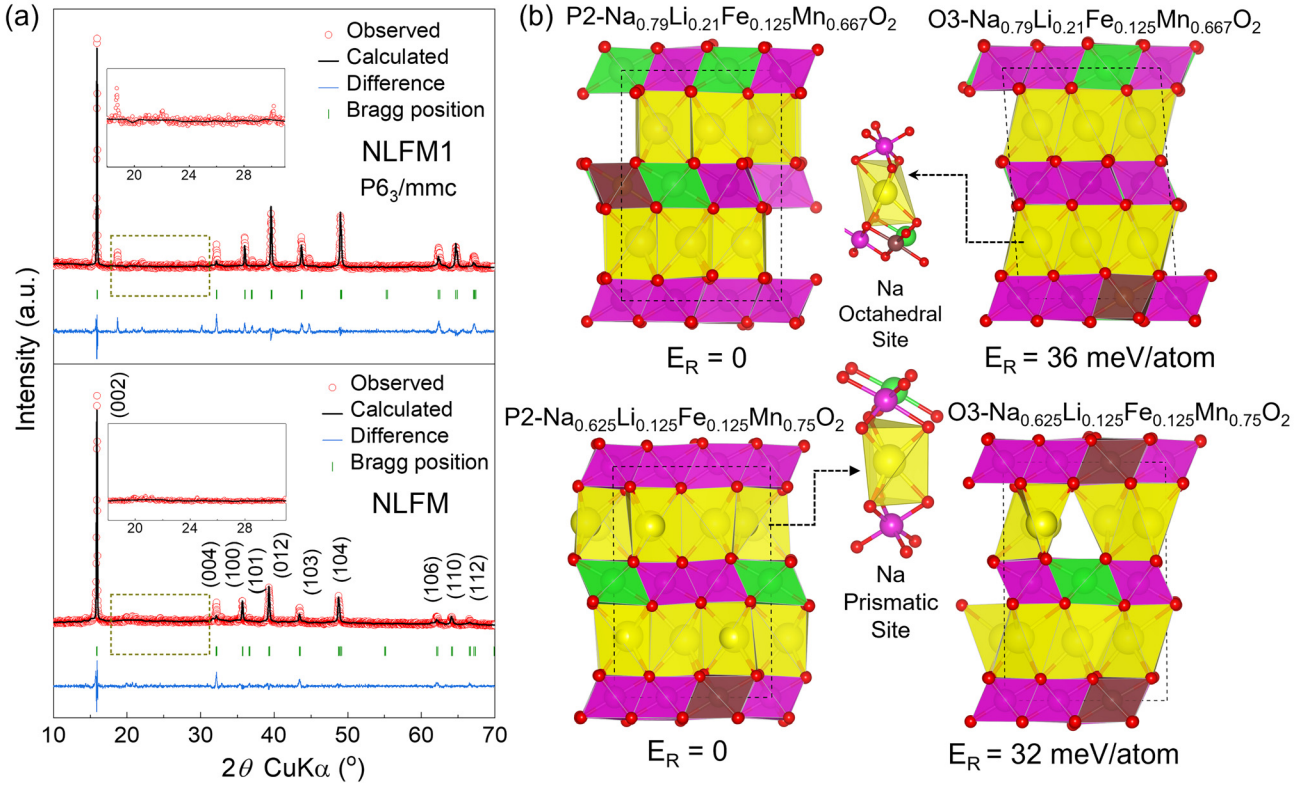

Fig. 1 (a) Rietveld refinements of the pristine NLFM1 and NLFM (top and bottom, respectively) with the inset in each showing the 2θ region of 18° to 31° for superstructure order in the TM layer, (b) comparison of the structural stability of P2 and O3 phases: the upper panel for $Na_{0.79}Li_{0.210}Fe_{0.125}Mn_{0.667}O_2$ (comparable to NLFM1), which has increased Li and Na contents, while the lower panel presents $Na_{0.625}Li_{0.125}Fe_{0.125}Mn_{0.75}O_2$ (comparable to NLFM). The respective relative energies are provided, indicating the thermodynamic phase stability of each configuration.

phase (Fig. S1b,† shows NLFM1 in the P2–O3 mixed phase when the synthesis temperature is altered).

By reducing the Na content and slightly increasing the Mn content, we were able to prepare the compound $Na_{0.7}Li_{0.127}Fe_{0.127}Mn_{0.746}O_2$ (NLFM), which lies well below the P2–O3 barrier line. Consequently, this compound is stable in the P2-phase (Fig. 1a, lower panel). The refined lattice parameters for the NLFM material are $a = b = 2.9017(2)$ Å and $c = 11.1295(3)$ Å, with a unit cell volume (V) = 81.15(6) Å^3 (Table S2a†). With 0.127 moles of Fe^{3+}, the material uses high voltage $Fe^{4+/3+}$ and anionic redox, yielding high energy density, as will be discussed in the following sections. In order to examine how the optimal Li and Fe stoichiometry affects the structural preference between the P2 and O3 phases, a comprehensive analysis based on DFT calculations was carried out. To assess the phase stability of two target materials, $Na_{0.625}Li_{0.125}Fe_{0.125}Mn_{0.125}(III)Mn_{0.625}(IV)O_2$ (comparable to NLFM) and $Na_{0.79}Li_{0.210}Fe_{0.125}Mn_{0.667}O_2$ (with a high Na content comparable to NLFM1), we compare the relative stability of their P2 and O3 phases. As shown in Fig. 1b, the O3 phase exhibits a higher relative energy than the P2 phase for both NLFM and NLFM1, indicating that in the presence of Li as a dopant the P2 phase is thermodynamically more favourable even in the presence of relatively higher Na in the material.

Stabilizing P2-type Na–Li–Fe–Mn–O in the low-Na limit during desodiation

Considering the higher reproducibility of synthesis of NLFM in the P2 phase we used this composition to further study the effect of Li^+ doping in the low-Na limit during desodiation.

NLFM structure and electrochemistry

Rietveld refinement results of neutron powder diffraction (NPD) of NLFM best fit to the space group $P6_3/mmc$ with a small amount (~3%) of Na_2CO_3 impurities (Fig. 2a and Table S2b†). Na_2CO_3 impurities probably arise due to the exposure of the sample to ambient air during sample preparation for NPD measurements.[15,16] Here, Na and Li/Mn/Fe atoms are alternately arranged within an oxygen framework, forming an ABBA-type hexagonal close-packed structure. The Na^+ ions occupy two types of prismatic coordination sites: Na_f (sharing faces with MO_6 octahedra) and Na_e (sharing edges with MO_6). Li^+ ions are found to reside in octahedral sites alongside Fe/Mn in adjacent transition metal (TM) layers. Both XRD and NPD refinements (Fig. 1a and 2a) clearly indicate the absence of any superstructure ordering of Li:TM in the TM layer. SEM images (Fig. S3a†) indicate that the particle size of the prepared samples ranges from 2 to 5 μm.

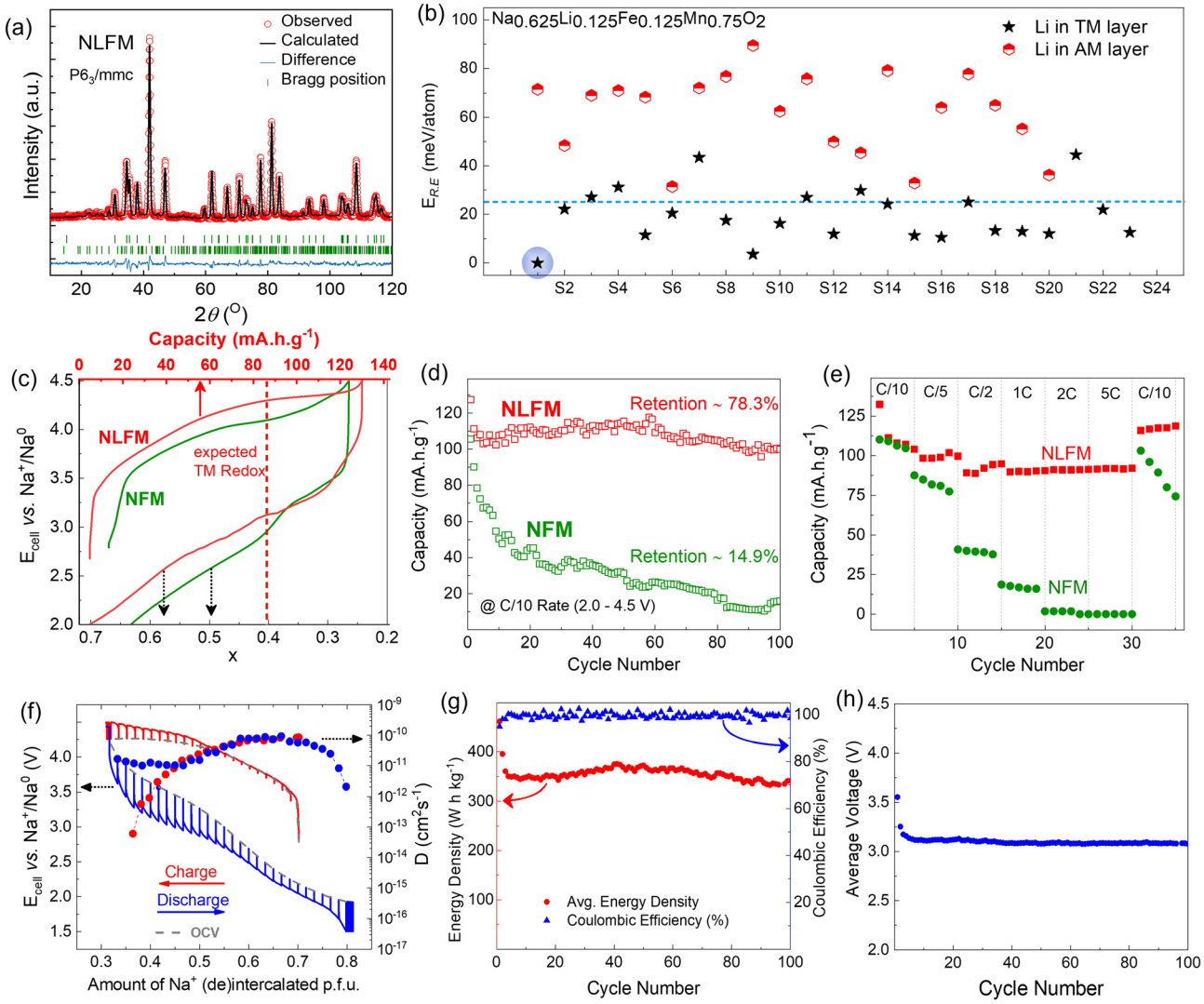

Fig. 2 (a) Neutron diffraction pattern of NLFM and its Rietveld refinement, (b) configurational stability of Li^+ in the alkali metal (AM) (red hexagons) and transition metal (TM) layers (black stars) for $Na_{0.625}Li_{0.125}Fe_{0.125}Mn_{0.125}(III)Mn_{0.625}(IV)O_2$. The most stable configuration is with Li^+ in the TM layer as highlighted in blue (S_0 in Fig. S4†). For NLFM: (c) typical charge–discharge profiles during the first cycle plotted with respect to the amount of Na retained in the structure at the C/10 rate, (d) capacity retention as a function of cycle number at the C/10 rate in the voltage range of 2.0–4.5 V, (e) rate capability with charge at the C/10 rate and discharge at 0.1C–5C, (f) GITT profiles and the corresponding diffusion coefficients (circles) during initial charging and discharging, (g) average energy density and coulombic efficiency as a function of cycle number at the C/10 rate in the voltage range of 2.0–4.5 V, and (h) average voltage *vs.* cycle number.

Thermogravimetric analysis (TGA) shows that the material is thermally stable, with only less than 6% mass loss up to 800 °C (Fig. S3b†). The loss can be accounted for by the absorbed moisture or Na_2CO_3 formation due to the exposure to ambient air.

The optimized P2-type structural arrangement of $Na_{0.625}Li_{0.125}Fe_{0.125}Mn_{0.75}O_2$ by DFT shows that Na ions occupy the trigonal prismatic coordination sites, while Li-ions occupy the octahedral coordination sites in the transition metal (TM) layer as shown in Fig. S3c.† To further identify the local structural arrangement and Li-TM ordering in $Na_{0.625}Li_{0.125}Fe_{0.125}Mn_{0.75}O_2$ as shown in Fig. S4 and Table S3,† we analyzed various structural configurations with different Li orderings with respect to Fe and Mn. Our findings indicate that many of these configurations have very similar energies, within approximately 25 meV per atom, comparable to the thermal energy (k_BT = 25.7 meV). This suggests that the Li-substituted framework does not adopt a single, well-defined ordering but instead exhibits a degree of configurational disorder, reinforcing the absence of a specific ordered framework. To assess the comparative suitability of Li occupying either the TM layer or the AM layer within the P2 framework, we analyze the relative energies of various configurations, as shown in Fig. S4 and S5.† As illustrated in Fig. 2b, most configurations with Li in the TM layer exhibit relative energies below 25 meV per atom, whereas configurations with Li in the AM layer have

relative energies exceeding this threshold. This pronounced energy difference indicates a stronger thermodynamic preference for Li to reside in the TM layer rather than the AM layer.

NLFM cathodes demonstrate an initial charge capacity of 128 mAh g^{-1} in the voltage range of 2.0–4.5 V, with a high coulombic efficiency of ~99.99% during galvanostatic charge/discharge cycling at C/10 current in the half-cell configuration (Fig. S2a and S2b†). Notably, the high initial charge capacity cannot be explained by TM redox reactions alone. Considering 0.127 moles of $Fe^{4+/3+}$ and 0.194 moles of $Mn^{4+/3+}$ each, approximately 88 mAh g^{-1} of the capacity arises from TM redox, while 40 mAh g^{-1} needs to be contributed by oxygen redox. This is also clearly evident in the cyclic voltammograms of NLFM (Fig. S7†). In contrast, the undoped $Na_{2/3}Fe_{0.5}Mn_{0.5}O_2$ (NFM) cathode shows a capacity of only 105 mAh g^{-1} with poorer coulombic efficiency and larger voltage hysteresis as compared to NLFM (Fig. 2c). While the NFM cathode retains only 14.9% of its initial capacity, NLFM retains >78% of its 1st cycling capacity after 100 cycles (Fig. 2d). In fact, beyond the first 2 cycles, the NLFM cathode retains >93% of its capacity. NLFM also shows lower voltage hysteresis as compared to the NFM cathode (Fig. 2c). To our surprise we find that the NLFM1 material, which had an initial high Na content of 0.80 moles, shows a poor capacity retention of only 38% after 100 cycles (Fig. S2d†). This aspect of the NLFM1 cathode is being studied in detail and is beyond the scope of this manuscript.

In the slow-charge–fast-discharge mode, the NLFM electrode exhibits excellent rate capability, showing an initial fall in capacity when discharged at C/10 but showing minimal capacity loss at higher rates (Fig. 2e). When the current rate returns to C/10, the NLFM electrode continues to deliver a reversible capacity of approximately 118 mAh g^{-1}, indicating good reversibility. Under fast-charge–fast-discharge conditions of 1C and 5C, the cathode retains close to 60% of the capacity after 200 cycles (Fig. S9†). Conversely, the NFM cathode shows a very fast decline of capacity with even a moderate current rate of C/2. The Na diffusion coefficient, D_{Na^+}, for NLFM lies in the range of 10^{-10} to 10^{-13} cm^2 s^{-1} during charge (Fig. 2f) and is sustained at 10^{-10} to 10^{-11} cm^2 s^{-1} during discharge. In contrast, the D_{Na^+} value of NFM and $Na_x[Li_{0.1}Fe_{0.37}Mn_{0.53}]O_2$ cathodes was found to decrease to 10^{-16} cm^2 s^{-1} at a voltage above 4.3 V.[9,17,18] For these cathodes, the drastic reduction of D_{Na^+} commences concurrently with the formation of an O-type phase.[9,19] This drastic reduction of D_{Na^+} is not observed for the NLFM cathode. NLFM also shows superior performance under higher cathode mass loading conditions (>15 mg cm^{-2}), maintaining an average cathode level energy density of about 350 Wh kg^{-1} (Fig. 2g), and an average voltage of 3.1 V (shown in Fig. 2h).

Absence of the O-phase in NLFM at the low-Na limit

Like most P2-type cathodes, NFM is known to exhibit phase transition from the hexagonal P2 phase to the O2 phase upon Na extraction above 4.2 V,[10,19] accompanied by a volume contraction of at least 12.6%. At critical Na concentrations of less than ~0.33 moles within the structure, the larger prismatic Na layers become unstable and the TMO_2 sheets slide to shrink the Na-layer to a smaller octahedral layer. This transition results in an 8.5% decrease in the lattice parameter in the *c*-direction (Fig. 3a and Table S8†). This phenomenon has been documented in the literature, with Nazar and group reporting the initial appearance of the "Z-phase" in NFM at approximately $x = 0.3$ (for $Na_xFe_{0.5}Mn_{0.5}O_2$).[8] In the case of P2-$Na_{0.67}Li_{0.1}Fe_{0.37}Mn_{0.53}O_2$,[9] the OP4 phase first emerges from $x = 0.27$ (O type peak starts emerging at $2\theta = 17.5°$) and the final charged phase at 4.5 V with $x = 0.22$ at $2\theta = 17.7°$ corresponding to a large volume change. Similar phase transitions have been reported for Mg doped and Ni doped cathodes as well.[6,10] In contrast, NLFM does not exhibit P2–OP4/O2 phase transition up to 4.5 V corresponding to the retention of about 0.25 moles of Na in the material (Fig. 3a). We observe gradual expansion of the *c*-axis during Na-deintercalation due to the electrostatic repulsion between the TMO_2 layers (Fig. S11†). At the end of the charging cycle, a negligible volume change of 1.8% is observed compared to the pristine sample. A more notable observation is that the sample collected at the end of the 1st and 100th discharge has only a marginal increase of 0.5–0.6% in volume compared to the pristine material, indicating high structural stability (Fig. S11†). On comparing the stability of $Na_{0.25}Li_{0.125}Fe_{0.125}Mn_{0.75}O_2$ (the high SOC state) in P2 and O3 phases we find that the P2 phase is thermodynamically more stable than the O3 phase (based on DFT studies, Fig. 3b). Moreover, the *c*-lattice parameter expands by ~1% (as detailed in Table S9†), consistent with experimental *ex situ* XRD observations.

To understand how the local structure in the material changes during charging and discharging, we extracted Extended X-ray Absorption Fine Structure (EXAFS) from hard X-ray Absorption Spectroscopy (XAS) at the Fe and Mn K-edge (Fig. S12†). The Fe–O bond length exhibits a slight decrease during charging, attributable to the formation of Fe^{4+}–O_6 octahedra. Notably, there is no substantial decline in the intensity of the scattering peaks (both TM–O and TM–TM) at either the Fe or Mn edge (Fig. 3c and d). Any migration of Fe or Mn ions or a distortion of the covalent environment around the Fe or Mn atoms due to the transition from the P-type to the O-type phase would be clearly visible as a change in the shape of the EXAFS features. A sharp decrease in the intensity of the scattering peaks has been reported for both undoped and Li/Mg doped $Na_{0.67}Fe_{0.5}Mn_{0.5}O_2$ on OP4 phase formation.[9,10] In order to further investigate the local electronic structure around the Fe, the *ex situ* ^{57}Fe Mössbauer spectra of the NLFM electrodes were recorded (Fig. 3e and f). The component shown in red displays an isomer shift (IS) of approximately 0.333 mm s^{-1} and a quadrupolar splitting (QS) of around 0.748 mm s^{-1}. These values are consistent with the Fe^{3+} in an octahedral environment. The component displayed in green exhibits an IS of ≈0.007 mm s^{-1} and a QS of ≈0.522 mm s^{-1}, corresponding to Fe^{4+}–O_6 octahedra (Table S10†). Quantitative analysis reveals a population ratio of Fe^{3+}–O_6 and Fe^{4+}–O_6 to be 71.8 : 28.2 for the charged NLFM cathode. No evidence of

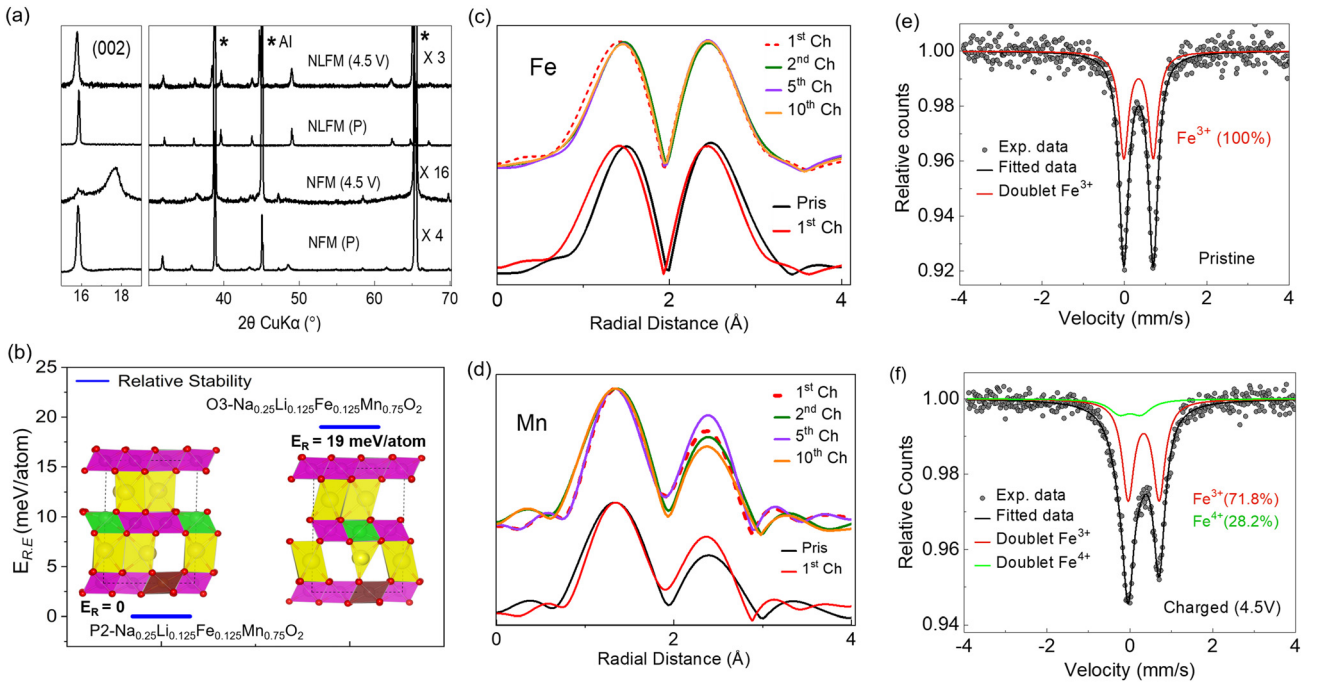

Fig. 3 (a) *Ex situ* XRD patterns of NFM and NLFM in their pristine (*P*) and charged (4.5 V) states, (b) relative structural stability of P-type and O-type phases in $Na_{0.25}Li_{0.125}Fe_{0.125}Mn_{0.75}O_2$ (based on DFT) is shown with their corresponding relative energies (E_R) in meV per atom, (c) Fe K-edge and (d) Mn K-edge EXAFS data extracted from hard XAS spectra collected at the end of the n^{th} charge (n = 1, 2, 5, and 10), and ^{57}Fe Mössbauer spectra of NLFM collected on (e) pristine and (f) the highest charge states (4.5 V). The fitted curves assigned to each Fe state and the percentages of each state are shown.

tetrahedral Fe^{3+}–O_4 or Fe^{4+}–O_4 is observed in the charged sample. Fe in NFM cathodes is known to reside at tetrahedral sites in the AM layer. In the OP4 phases reported earlier, for example, in fully charged $Na_{0.67}Li_{0.1}Fe_{0.37}Mn_{0.53}O_2$, clear evidence of two different Fe^{3+} and two different Fe^{4+} phases is observed upon fitting the hyperfine splitting, indicative of the migration of Fe^{4+} ions.[9,20]

Redox processes and their reversibility upon Li-doping

As demonstrated by the ^{57}Fe Mössbauer data, only a small fraction of Fe^{3+} converts to Fe^{4+} at the culmination of the charging process to 4.5 V. XAS studies were conducted at the Fe and Mn K-edge to investigate the redox mechanism. The pristine sample exhibited an edge position comparable to the Fe_2O_3 standard, indicating an initial Fe oxidation state of Fe^{3+} (Fig. S12a†). During the process of Na deintercalation, the Fe K-edge spectrum underwent a shift in edge energy towards higher values and subsequently reverted fully upon discharge over the course of multiple charge–discharge cycles (Fig. S13†), thereby suggesting the reversible return of Fe^{4+} to Fe^{3+}. Of particular significance is the absence of any new pre-edge feature formation throughout the charge–discharge cycle, which confirms that there is no significant distortion in the environment around Fe and no irreversible migration of Fe.[20] During the initial charge, the Mn K-edge energy does not change drastically but shifts to lower energies upon discharging to 2.0 V. Due to the inherent complexity of the Mn K-edge spectrum, it is difficult to directly determine the exact expected change in edge energy upon Mn oxidation. Nevertheless, the observed changes in the pre-edge peak intensity serve as a reliable indicator of Mn oxidation during the initial charge cycle.

XAS at the O K-edge displays an enhancement in the pre-edge intensity when compared to the pristine state (Fig. 4a). Based on previous studies we assign the 528–530 eV regions to the formation of delocalized hole states on O 2p orbitals (here, significantly overlapped with the TM-t_{2g} orbital at 530 eV), while the increase of intensity around the 531 eV region would indicate the formation of localized molecular-like O 2p states, respectively.[21] Upon discharge, the incoming electrons are redistributed over the entire pre-edge region. It is noteworthy that the material exhibits reversible O-redox over multiple cycles, as evidenced by the similarity of the O–K edge spectra of the samples at the conclusion of the 2nd and 5th charge cycles. There is an overall decrease in the hole states in the pre-edge region when compared to the 1st charge cycle (possibly because of some O-loss in the 1st charge cycle). We acknowledge that the high voltage stability of the electrolyte may be a contributing factor to the observed minimal O-loss during the initial cycle. Additional electrolyte optimization, therefore, has the potential to further improve the cathode performance. The resonant inelastic X-ray scattering (RIXS) spectra were extracted at an excitation energy range of 531.3 eV from the RIXS maps collected in the O 2p pre-edge region. For the charged samples, O–O stretching vibrations appear in the

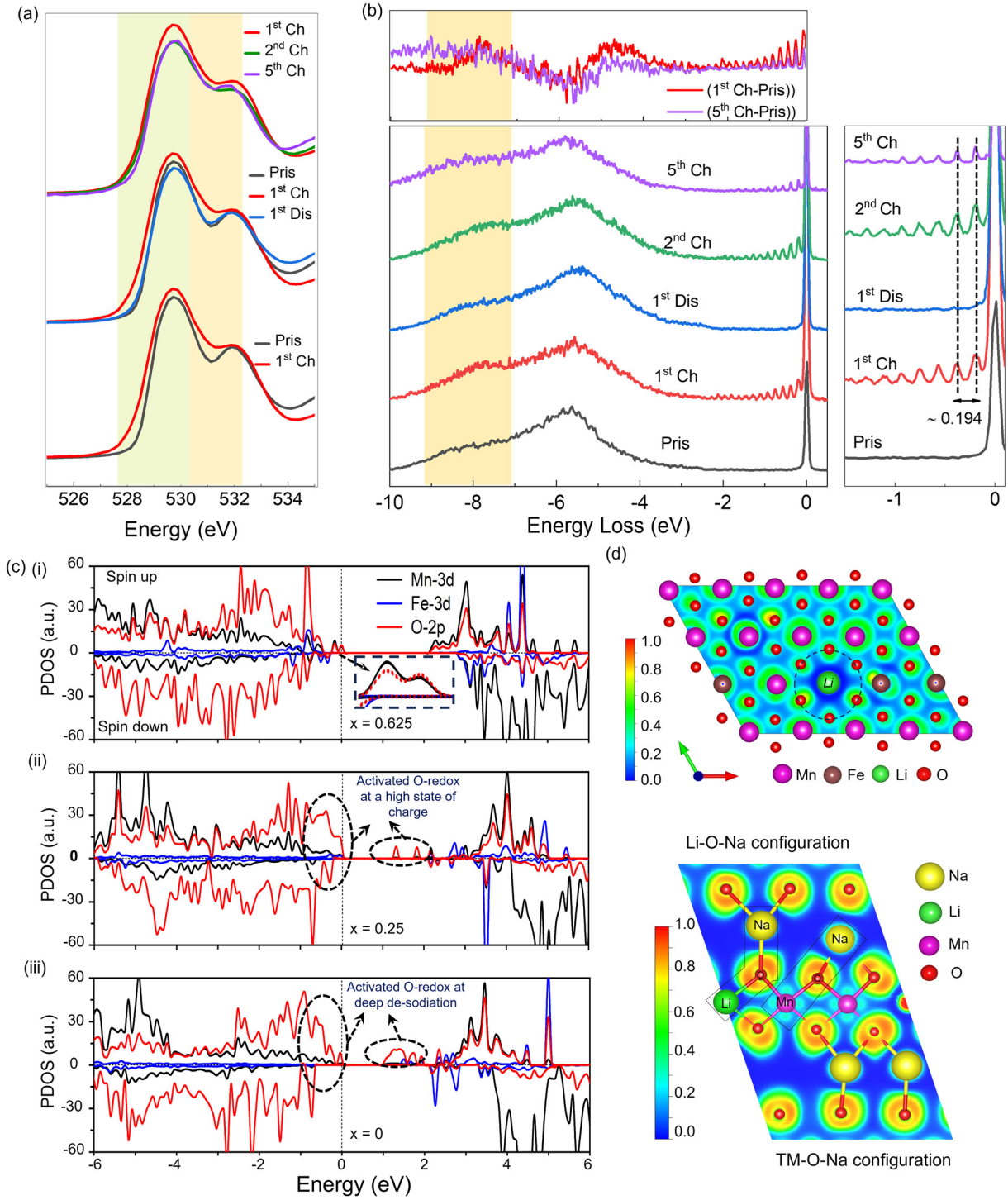

Fig. 4 (a) Oxygen K edge XAS spectra collected in TFY mode on pristine, charged and discharged samples collected at the *n*th cycle (*n* = 1, 2, 5), (b) RIXS line spectra of the same collected at an excitation energy of 531.3 eV. The right panel in (b) shows the elastic region of the same RIXS spectra and the top panel shows the difference spectra of charged and pristine samples. (c) Electronic structure evolution: projected density of states (pDOS) was computed using the HSE06 hybrid functional with a screening parameter of ω = 0.11 Å^{-1} for Mn-3d, Fe-3d, and O-2p orbitals in P2-$Na_xLi_{0.125}Fe_{0.125}Mn_{0.125}(III)Mn_{0.625}(IV)O_2$ at (i) x = 0.625, (ii) x = 0.25, and (iii) x = 0. The Fermi energy is set to 0 eV. (d) Electron localization function (ELF) plots of P2-$Na_{0.625}Li_{0.125}Fe_{0.125}Mn_{0.75}O_2$, illustrate the ionic character of Li–O compared to the transition metal (TM)–O bonds.

vicinity of the elastic peak and disappear on discharge but reappear, albeit with a decrease in intensity, on subsequent charge. The −8 eV energy loss feature, understood to be a hallmark of O-redox, appears and disappears during the charge and discharge cycles, respectively (Fig. 4b and S14†).[22] The intensity of the signature inelastic feature at around −8 eV after the 5th charge remains comparable to that of the 1st charge, as clearly evident from the difference spectra derived from the 531 eV excitation spectrum of the charged samples (top inset in Fig. 4b). To understand the role of lithium orbital hybridization in anionic redox reactions at a high SOC, the projected density of states (pDOS) and Bader charge analysis were carried out using a hybrid-level DFT approach. The pDOSs at high SOCs and the corresponding average Bader charges for oxygen in $Na_xLi_{0.125}Fe_{0.125}Mn_{0.75}O_2$ are presented in Fig. 4c and Table S9.† The valence band maxima for the composition with $x = 0.625$ are predominantly contributed by Mn-3d states, indicating that the initial charge compensation occurs mainly through Mn redox upon sodium extraction. As the SOC increases ($x = 0.25$), a significant increase in O-2p states is observed near the Fermi level, signalling the contribution from anionic redox activity. At complete sodium depletion ($x = 0$), the O-2p states remain dominant at the top of the valence band, with an even greater presence of unoccupied O-2p states. The average Bader charges on oxygen further reinforce this charge compensation mechanism during Na^+ deintercalation, in agreement with the pDOS analysis. These findings underscore the crucial role of O-2p electrons in facilitating charge compensation under deep states of desodiation.

It is to be stated here that we can clearly see the activation of O-redox in NLFM even without undergoing any structural phase transition. To the best of our knowledge this phenomenon is hitherto unknown, and O-redox has always been associated with structural transitions. For example, the highly covalent nature of TM–O bonds in the NFM cathode would lead to strong electron sharing between TM and O. Therefore, O-redox gets activated only upon formation of ionic □–O–□ (or Na–O–□). This happens only when one of the TM ions migrates from the TM layer to the Na layer, which would invariably require P to O type phase transition.[10] To further understand the origin of the O-redox phenomenon in NLFM without the formation of □–O–□, we plot the electron localization function (ELF) along the (001) plane for $Na_{0.625}Li_{0.125}Fe_{0.125}Mn_{0.75}O_2$. Fig. 4d illustrates the distinctly different ionic characteristics when comparing Li–O and transition metal (TM)–O bonds. Incorporation of Li into the Fe–Mn-based framework enhances the ionic character of the Na–O–Li configuration compared to the Na–O–TM configuration (Fig. 4d, bottom panel), significantly modifying the electronic structure. The electron density distribution on framework oxygen is influenced by its local coordination environment. In the Li–O–Na configuration, oxygen exhibits enhanced electron density, and a distinct spatial orbital distribution compared to its behavior in the TM–O–Na configuration. This difference suggests that the presence of Li in the framework possibly enables tunable O-redox behavior. To probe the ionicity and covalency in the $Na_{0.625}Li_{0.125}Fe_{0.125}Mn_{0.75}O_2$ structure, the ELF was computed as shown in Fig. 4d. A two-dimensional ELF contour plot displayed higher ELF values for TM and oxygen atoms, revealing the covalent bonding mechanism of TM–O bonds. In contrast, lower ELF values (blue regions) were observed around Li in the Li–O bonds, indicating their predominantly ionic character due to significant electron localization on oxygen rather than lithium. The Na–O–Li configuration has been reported to enhance anionic redox activity, as demonstrated by Wang *et al.*[23] In their study, the high ionicity of the Li–O bond was shown to promote the formation of unhybridized O 2p states, thereby enabling reversible oxygen redox processes, corroborating the case studied by us too. It is therefore evident that the highly ionic character of Li–O bonds in NLFM increases the electron density over O orbitals, making O-redox feasible in the P2-phase even in the absence of □–O–□.

Discussions on the role of Li in stabilizing the P2 phase

It is important to note here that many strategies have been adopted previously to prevent P2–O2 phase transition in Fe–Mn based cathodes. One of the most popularly adopted strategies has been to dope with small quantities of Ni^{2+} owing to its higher octahedral site stabilization energy as compared to Fe.[8] Fe^{4+} ions still migrate to the O-type AM layer and some of them get trapped, leading to voltage fade. These transitions occur at deep states of desodiation and for this reason, most previous studies have limited the operating window of 2.0–4.0 V to avoid the P2–O2 transition. Initial studies on doping with Mg^{2+} proved to be effective at increasing the overall redox; however, at a high SOC Mg^{2+} migrates and gets trapped in the O-type layer.[10]

To investigate the impact of the optimal Li composition on Na/TM ion migration and TM layer gliding, *ab initio* molecular dynamics (AIMD) simulations were performed on $Na_xLi_{0.125}Fe_{0.125}Mn_{0.875}O_2$ at varying SOCs ($x = 0.625$ and 0.25) and on $Na_{0.79}Li_{0.210}Fe_{0.125}Mn_{0.667}O_2$, as well as on Li-free frameworks P2-$Na_xFe_{0.125}Mn_{0.875}O_2$ and ($x = 0.25$ and 0.67). Fig. 5a illustrates the fine-tuning of Na^+ mean square displacement (MSD) at 800 K in $Na_{0.625}$ $Li_{0.125}Fe_{0.125}Mn_{0.875}O_2$ compared to its Li-free analogue. Higher Na^+-MSD in $Na_{0.625}Li_{0.125}Fe_{0.125}Mn_{0.875}O_2$ (representing NLFM) compared to $Na_{0.79}Li_{0.210}Fe_{0.125}Mn_{0.667}O_2$ (representing NLFM1) reflects the superior rate performance of the former, consistent with experimental observations. To understand the reason for high Na^+ diffusion, the van Hove correlation function of Na^+ in both compositions is explored (shown in Fig. 5b and c) based on ionic trajectories from AIMD simulation at 800 K. The red peak (for $Na_{0.625}Li_{0.125}Fe_{0.125}Mn_{0.875}O_2$) in the self-part ($G_s$) between 0 and 2.0 Å corresponds to the shortest Na–Na distances, as seen in Fig. 5b. This distance increases rapidly after ~10 ps and becomes nearly uncorrelated after 30 ps, indicating that Na^+ ions readily migrate from their initial positions to neighbouring Na^+ sites. In contrast, for the Na = 0.79 cathode (NLFM1), the peak in G_s between 0 and 2.0 Å remains stable for up to 40 ps, significantly longer than in Na = 0.625

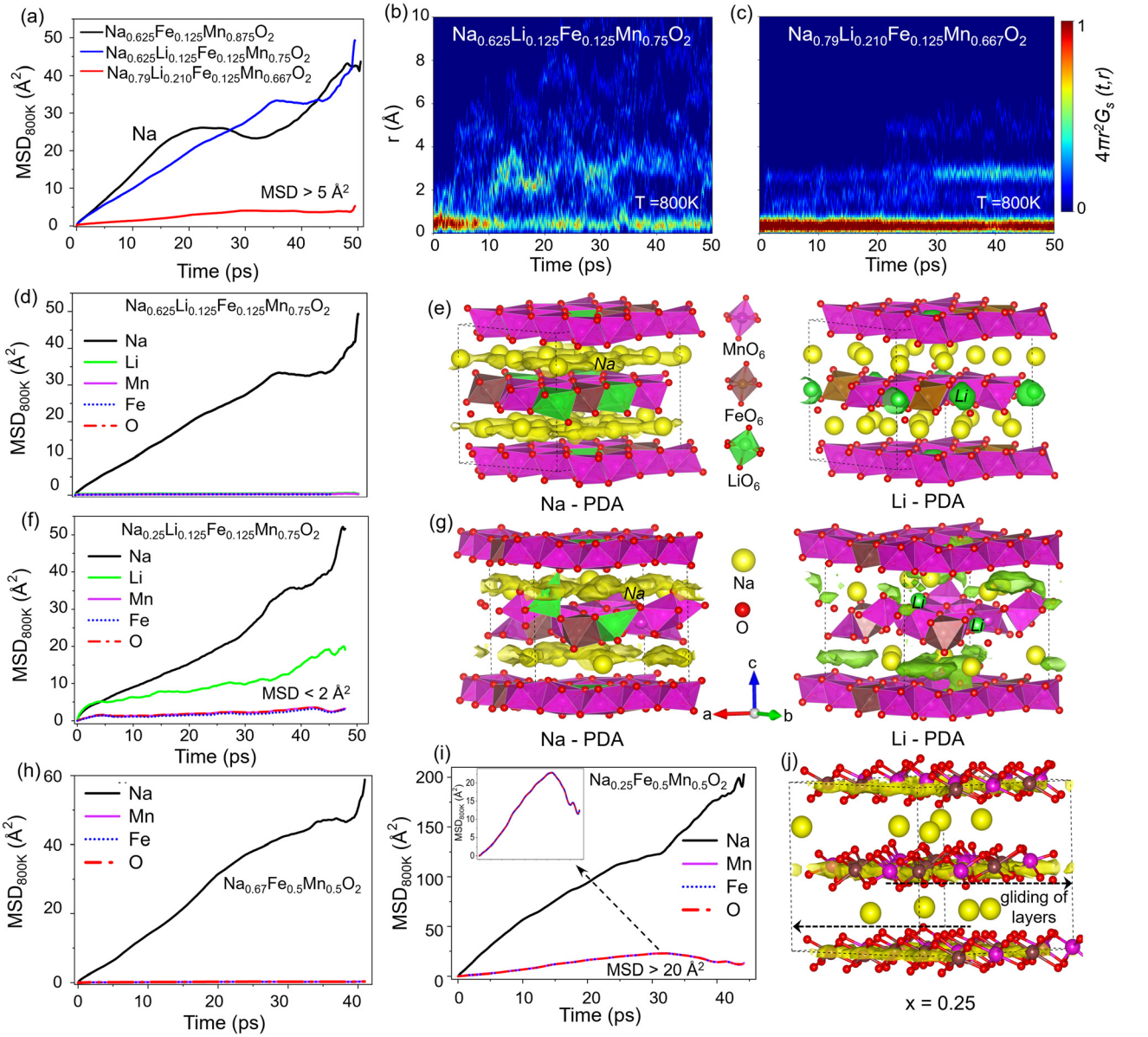

Fig. 5 Ionic diffusion properties. (a) Mean square displacement (MSD) for Na-ions as a function of time at 800 K for Li-free P2-$Na_{0.625}Fe_{0.125}Mn_{0.875}O_2$, and Li containing P2-$Na_{0.625}Li_{0.125}Fe_{0.125}Mn_{0.125(III)}Mn_{0.625(IV)}O_2$ (P2-NLFM), and P2-$Na_{0.79}Li_{0.210}Fe_{0.125}Mn_{0.667}O_2$ (P2-NLFM1) frameworks. The self-part of the van Hove correlation function (G_s) for sodium in (b) P2-NLFM and (c) P2-NLFM1 as a function of the average Na–Na pair distance (r) and time step at 800 K. Species resolved MSD of Na, Li, Mn, Fe, and O as a function of time at 800 K in P2-NLFM for (d) x = 0.625 (discharged state) and (f) x = 0.25 (charged state). Probability density distribution function $P(r)$ of Na^+ and Li^+ ions in P2-NLFM for (e) x = 0.625 and (g) x = 0.25, obtained from an AIMD trajectory of 50 ps at 800 K. The isosurface value is set to 0.0045 $bohr^{-3}$, where the yellow isosurface represents Na^+-PDA and the green isosurface indicates Li^+-PDA, (h) mean squared displacement (MSD) of Na, Mn, Fe, and O as a function of time at 800 K in P2-$Na_xFe_{0.5}Mn_{0.5}O_2$ for (h) x = 0.67 and (i) x = 0.25 (charged state), and the inset highlights the coupled motion of transition metals and oxygen in P2-$Na_{0.25}Fe_{0.5}Mn_{0.5}O_2$, and (j) probability density distribution function $P(r)$ in P2-$Na_{0.25}Fe_{0.5}Mn_{0.5}O_2$, capturing the in-plane motion of Mn, Fe, and oxygen.

(NLFM), suggesting that the Na^+ ions in Na = 0.79 (NLFM1) are less prone to diffusion to adjacent sites. Note that we clearly observe peaks in the XRD pattern due to Li:TM superstructure ordering (Fig. 1a, a 2θ region of 18° to 31°) in the NLFM1 material.[22,24,25] An ordered TM layer will possibly induce Na to undergo order–disorder transitions (even if at a local level), thereby reducing the Na-diffusivity.

To assess the dynamic stability of NLFM at different states of charge (Na = 0.25 and 0.625), the MSD of each ionic species was carefully analyzed at 800 K, as shown in Fig. 5d and f. At a high Na concentration (Na = 0.625), both Li and TM ions show negligible displacement, indicating structural stability. In contrast, at a low Na concentration (Na = 0.25), we tracked Li migration from the TM layers into the AM layers along with

two-dimensional (2D) in-plane Na diffusion. Notably, the transition metal ions maintain an MSD of less than 2 Å within an AIMD time scale of 50 ps. A similar phenomenon has been proposed for a Li-doped O3-type Na-ion cathode, *i.e.*, Li^+ migrates preferentially to Fe.[26] This suggests that at a high SOC, dynamic and reversible Li migration between TM and AM layers prevents layer-gliding and stabilizes the P2-type configuration of NLFM. To gain more intuitive insights, the probability density function $P(r)$ of Na and Li at 800 K, derived from AIMD simulation for NLFM at different SOCs, is illustrated in Fig. 5e and g. It reveals that Na^+ ions exhibit 2D in-plane diffusion, with interconnected diffusion channels at both high and low SOCs (Na = 0.625 and 0.25). In contrast, Li^+ ions show mostly localized, static motion in the discharge state (Na = 0.625), but at a high charge state (Na = 0.25), they exhibit out-of-plane motion with limited long-range diffusion in the AM layer. In addition, an analysis of species-resolved MSD in high Fe containing P2-$Na_xFe_{0.5}Mn_{0.5}O_2$ (x = 0.25 and 0.67) frameworks was conducted using AIMD trajectories at 800 K, as shown in Fig. 5(h–j) and S15.† The results revealed that despite high Na-ion diffusion, a significant coupled motion of TM and oxygen atoms was observed at a high SOC. The MSD for framework ions (Mn, Fe, and O) exceeded 20 $Å^2$, and the probability density plot confirms the in-plane movement of TM and oxygen atoms (Fig. 5i and j), indicating TM layer gliding, which ultimately drives phase transitions.

The coupled motion of TM and O in MSD plots of NFM cathodes at x = 0.25 matches well with the experimental observation of O-phase formation in XRD at x = 0.27 (=4.5 V charge). It is noteworthy that Li doping as a strategy to counter the P to O type phase transition has been previously attempted. Our results indicate that not just the presence of Li but also its proportion in relation to Fe and Mn in the system are critical. Consequently, the P2 cathode with a composition of P2-$Na_{0.67}Li_{0.1}Fe_{0.37}Mn_{0.53}O_2$ [9] *i.e.*, a lower Li content and higher Fe content than NLFM, undergoes substantial O-phase formation with 0.26 Na present in the structure. For NLFM we do not observe any O-phase formation, even at x close to 0.21 moles (Fig. S16†). This indicates that the stoichiometry of both Li and Fe in the structure plays a significant role in determining the stability of the P2 phase. For example, for $Na_{0.67}Li_{0.1}Fe_{0.37}Mn_{0.53}O_2$ [9] with a higher proportion of Fe in the cathode, Fe migration again becomes feasible (in addition to Li-migration) at a high SOC (Na < 0.27) and OP4 phase transition ensues. Our observations suggest that Na–Li–Fe–Mn–O cathodes with significantly lower proportion of Fe (close to 0.125 moles per f.u.) compared to Mn (0.7 or greater) can maintain the P2 phase over a broad range of Na compositions. Furthermore, AIMD trajectories conducted on P2-$Na_{0.25}Li_{0.125}Fe_{0.125}Mn_{0.125}(III)Mn_{0.625}(IV)O_2$ cathodes exhibit a high propensity of Li to migrate dynamically between TM and AM layers, while for the same cathode at a low SOC (x = 0.625), the Li shows static motion and remains mostly localized in the TM layer. This observation signifies that at a high SOC, a dynamic species, such as Li, easily migrates between the O-type TM layer and the P-type AM layer and will therefore be more effective in preventing P–O migration than simply limiting the voltage window to retain enough Na in the AM layers.

It is important to acknowledge that earlier studies on Li-doped Na–Fe–Mn–O cathodes, such as $Na_{0.66}Li_{0.18}Fe_{0.12}Mn_{0.7}O_2$ [27] and $Na_{0.6}Li_{0.11}Fe_{0.27}Mn_{0.62}O_2$,[28] have concluded that there is an absence of O2 phase formation. However, these studies have indicated a contraction of the lattice in the c-direction when the material is charged to 4.5 V. These articles do not provide a satisfactory explanation for the possible origin of lattice contraction in the absence of O-type phase formation. No such lattice contraction is observed for NLFM cathodes, which suggests that the P2 phase is fully retained. In fact, the lattice expands by approximately 0.25% in the c-direction upon charging to 4.5 V, attributable to O–O repulsions with Na loss from the AM layer.

Conclusions

We show that the incorporation of Li-ions in P2-Na–Fe–Mn–O cathodes can prevent the O-type phase formation both at high SOCs *i.e.*, at low-Na-stoichiometry and high-Na-stoichiometry. At low Na-stoichiometry, partially mobile Li^+ can reversibly migrate between octahedral TM layers and prismatic AM layers, thereby hindering layer gliding. While in the high-Na-stoichiometry region, the presence of Li^+ increases the Mn valence state, thereby increasing the cationic potential of the TM layer and thus stabilizing the material well below the P2–O3 transition barrier line. The proportion of Li to Fe and Mn within the structure is also of significance. Cathodes that exhibit an optimal Li : Fe : Mn ratio with a low proportion of Fe compared to Mn (close to 0.125 : 0.125 : 0.75) can maintain the P2 phase over a broad range of Na compositions. This enables the utilization of a large voltage window, particularly in the high voltage range above 4 V, where the majority of the Fe and O redox reactions occur. In the absence of O-phase formation, the cathode exhibits a negligible volume change and facile Na kinetics and, more crucially, ensures high-capacity retention. By eliminating high-voltage structural transitions and associated volume changes, a Li-doped Na–Fe–Mn–O cathode can make the high-voltage redox processes, such as $Fe^{4+/3+}$ and O-redox, reversible. Our study, therefore, proposes Li-doping as a strategy for harnessing the P2 phase in the Na–Fe–Mn–O cathode over a large compositional space, thereby ensuring a large energy density along with high capacity retention.

Author contributions

AG and UM conceptualized the project and carried out majority of the data analysis, AG carried out majority of the experiments, VST and SB conceptualized and carried out the DFT and AIMD studies with assistance from VM, SP assisted AG in *ex situ* sample preparation, SSM carried out the Mössbauer experiments and analysis, MH, LD, PT, AG, CS, and

TT assisted with the RIXS and O–K edge XAS beamtime experiments at VERITAS, SDK carried out the NPD experiment and refinement, TD assisted with the Mn and Fe K-edge XANES experiments at the beamtime, SG assisted with XANES and EXAFS analysis, and UM and AG compiled and wrote the manuscript with assistance from all other authors.

Conflicts of interest

There are no conflicts to declare.

Data availability

Data supporting the findings in the present work are available in the manuscript and its ESI.†

Acknowledgements

UM acknowledges support from the SERB (SPG/2021/000033) grant, AG is grateful for the DST INSPIRE fellowship, and SB acknowledges support from the SERB (CRG/2022/009476) and the CSIR for the 01WS(013)/2023-24/EMR-II/ASPIRE research grant. VST is grateful for an MHRD research fellowship. We acknowledge NSM, C-DAC, and MeitY for the HPC facilities (PARAM Ganga) at IIT Roorkee. Part of this research was conducted at PETRA III, and we gratefully acknowledge the staff for their assistance in using Beamline P65 and the financial support for the travel to attend the beamtime from DST's India@DESY collaboration. We would like to thank the staff of MAX IV Laboratory for the stable operation of the synchrotron during the experiment under proposal no. 20240481.

References

1 C. Zhao, Z. Yao, Q. Wang, H. Li, J. Wang, M. Liu, S. Ganapathy, Y. Lu, J. Cabana, B. Li, X. Bai, A. Aspuru-Guzik, M. Wagemaker, L. Chen and Y.-S. Hu, *J. Am. Chem. Soc.*, 2020, **142**, 5742.
2 N. A. Katcho, J. Carrasco, D. Saurel, E. Gonzalo, M. Han, F. Aguesse and T. Rojo, *Adv. Energy Mater.*, 2016, **7**, 1601477.
3 C. Delmas, C. Fouassier and P. Hagenmuller, *Physica B+C*, 1980, **99**, 81.
4 N. Yabuuchi, K. Kubota, M. Dahbi and S. Komaba, *Chem. Rev.*, 2014, **114**, 11636.
5 N. Yabuuchi, M. Kajiyama, J. Iwatate, H. Nishikawa, S. Hitomi, R. Okuyama, R. Usui, Y. Yamada and S. Komaba, *Nat. Mater.*, 2012, **11**, 512.
6 J. W. Somerville, A. Sobkowiak, N. Tapia-Ruiz, J. Billaud, J. G. Lozano, R. A. House, L. C. Gallington, T. Ericsson, L. Häggström, M. R. Roberts, U. Maitra and P. G. Bruce, *Energy Environ. Sci.*, 2019, **12**, 2223.
7 X. Li, Y. Wang, D. Wu, L. Liu, S.-H. Bo and G. Ceder, *Chem. Mater.*, 2016, **28**, 6575.
8 E. Talaie, V. Duffort, H. L. Smith, B. Fultz and L. F. Nazar, *Energy Environ. Sci.*, 2015, **8**, 2512.
9 X. Wang, Q. Zhang, C. Zhao, H. Li, B. Zhang, G. Zeng, Y. Tang, Z. Huang, I. Hwang, H. Zhang, S. Zhou, Y. Qiu, Y. Xiao, J. Cabana, C.-J. Sun, K. Amine, Y. Sun, Q. Wang, G.-L. Xu, L. Gu, Y. Qiao and S.-G. Sun, *Nat. Energy*, 2024, **9**, 184.
10 E. Boivin, R. A. House, J. Marie and P. G. Bruce, *Adv. Energy Mater.*, 2022, **12**, 2200702.
11 C. Zhao, Q. Wang, Z. Yao, J. Wang, B. Sánchez-Lengeling, F. Ding, X. Qi, Y. Lu, X. Bai, B. Li, H. Li, A. Aspuru-Guzik, X. Huang, C. Delmas, M. Wagemaker, L. Chen and Y.-S. Hu, *Science*, 2020, **370**, 708.
12 C. Chen, W. Huang, Y. Li, M. Zhang, K. Nie, J. Wang, W. Zhao, R. Qi, C. Zuo, Z. Li, H. Yi and F. Pan, *Nano Energy*, 2021, **90**, 106504.
13 M. Bianchini, E. Gonzalo, N. E. Drewett, N. Ortiz-Vitoriano, J. M. L. Del Amo, F. J. Bonilla, B. Acebedo and T. Rojo, *J. Mater. Chem. A*, 2018, **6**, 3552.
14 L. Yang, J. M. L. Del sAmo, Z. Shadike, S. Bak, F. Bonilla, M. Galceran, P. K. Nayak, J. R. Buchheim, X. Yang, T. Rojo and P. Adelhelm, *Adv. Funct. Mater.*, 2020, **30**, 2003364.
15 W. Zuo, Z. Xiao, M. Zarrabeitia, X. Xue, Y. Yang and S. Passerini, *ACS Mater. Lett.*, 2022, **4**, 1074.
16 W. Zuo, J. Qiu, X. Liu, F. Ren, H. Liu, H. He, C. Luo, J. Li, G. F. Ortiz, H. Duan, J. Liu, M.-S. Wang, Y. Li, R. Fu and Y. Yang, *Nat. Commun.*, 2020, **11**, 3544.
17 Z. Wang, S. Zhang, X. Fu, R. Huang, L. Huang, J. Zhang, W. Yang, F. Fu and S. Sun, *ACS Appl. Mater. Interfaces*, 2024, **16**, 2378.
18 D. Nayak, T. Sarkar, N. V. P. Chaudhary, M. D. Bharadwaj, S. Ghosh and V. Adyam, *J. Solid State Electrochem.*, 2017, **22**, 1079.
19 Q. Shen, X. Zhao, Y. Liu, Y. Li, J. Zhang, N. Zhang, C. Yang and J. Chen, *Adv. Sci.*, 2020, **7**, 2002199.
20 X. Gao, L. Fang, H. Wang, S. Lee, H. Liu, S. Zhang, J. Gao, Y. Mei, M. Park, J. Zhang, M. Chen, L. Zhou, W. Deng, G. Zou, H. Hou, Y. Kang and X. Ji, *Adv. Funct. Mater.*, 2022, **33**, 2212685.
21 U. Maitra, R. A. House, J. W. Somerville, N. Tapia-Ruiz, J. G. Lozano, N. Guerrini, R. Hao, K. Luo, L. Jin, M. A. Pérez-Osorio, F. Massel, D. M. Pickup, S. Ramos, X. Lu, D. E. McNally, A. V. Chadwick, F. Giustino, T. Schmitt, L. C. Duda, M. R. Roberts and P. G. Bruce, *Nat. Chem.*, 2018, **10**, 288.
22 R. A. House, U. Maitra, M. A. Pérez-Osorio, J. G. Lozano, L. Jin, J. W. Somerville, L. C. Duda, A. Nag, A. Walters, K.-J. Zhou, M. R. Roberts and P. G. Bruce, *Nature*, 2019, **577**, 502.
23 H. Dong, H. Liu, Y.-J. Guo, Y.-H. Feng, X. Zhu, S.-W. Xu, F. Sui, L. Yu, M. Liu, J.-Z. Guo, Y.-X. Yin, B. Xiao, X.-L. Wu, Y.-G. Guo and P.-F. Wang, *J. Am. Chem. Soc*, 2024, **146**, 22335.

24 Y. Yu, Q. Mao, D. Wong, R. Gao, L. Zheng, W. Yang, J. Yang, N. Zhang, Z. Li, C. Schulz and X. Liu, *J. Am. Chem. Soc.*, 2024, **146**, 22220.
25 Z.-X. Huang, X.-L. Zhang, X.-X. Zhao, H.-Y. Lü, X.-Y. Zhang, Y.-L. Heng, H. Geng and X.-L. Wu, *J. Mater. Sci. Technol.*, 2023, **160**, 9.
26 Y. Niu, Z. Hu, H. Mao, L. Zhou, L. Wang, X. Lou, B. Zhang, D. Xiao, Y. Yang, F. Ding, X. Rong, J. Xu, W. Yin, N. Zhang, Z. Li, Y. Lu, B. Hu, J. Lu, J. Li and Y.-S. Hu, *Energy Environ. Sci.*, 2024, **17**, 7958.
27 L. Yang, X. Li, J. Liu, S. Xiong, X. Ma, P. Liu, J. Bai, W. Xu, Y. Tang, Y.-Y. Hu, M. Liu and H. Chen, *J. Am. Chem. Soc.*, 2019, **141**, 6680.
28 M.-H. Cao, R.-Y. Li, S.-Y. Lin, S.-D. Zheng, L. Ma, S. Tan, E. Hu, Z. Shadike, X.-Q. Yang and Z.-W. Fu, *J. Mater. Chem. A*, 2021, **9**, 27651.